ACS APPLIED MATERIALS & INTERFACES
Research Article
www.acsami.org

Ferroelectric Properties of Vertically Aligned Nanostructured $BaTiO_3$–CeO_2 Thin Films and Their Integration on Silicon

Fauzia Khatkhatay,[†] Aiping Chen,[†] Joon Hwan Lee,[‡] Wenrui Zhang,[‡] Haron Abdel-Raziq,[†] and Haiyan Wang*,[†,‡]

[†]Department of Electrical and Computer Engineering, Texas A&M University, College Station, Texas 77843-3128, United States
[‡]Materials Science and Engineering Program, Texas A&M University, College Station, Texas 77843-3003, United States

ABSTRACT: Epitaxial $(BaTiO_3)_{0.5}(CeO_2)_{0.5}$ films have been deposited in vertically aligned nanocomposite form on $SrTiO_3$/TiN buffered Si substrates to achieve high-quality ferroelectrics on Si. The thin TiN seed layer promotes the epitaxial growth of the $SrTiO_3$ buffer on Si, which in turn is essential for the high-quality growth of the vertically aligned nanocomposite structure. X-ray diffraction and transmission electron microscopy characterization show that the films consist of distinct *c*-axis oriented $BaTiO_3$ and CeO_2 phases. Polarization measurements show that the $BaTiO_3$–CeO_2 films on Si are actually ferroelectric at room temperature, and the ferroelectric response is comparable to pure $BaTiO_3$ as well as the $BaTiO_3$–CeO_2 films on $SrTiO_3$ single-crystalline substrates. Capacitance-voltage measurements show that, instead of decreasing, the Curie temperature increases to 175 and 150 °C for the samples on $SrTiO_3$ and Si substrates, respectively. This work is an essential step towards integrating novel nanostructured materials with advanced functionalities into Si-based devices.

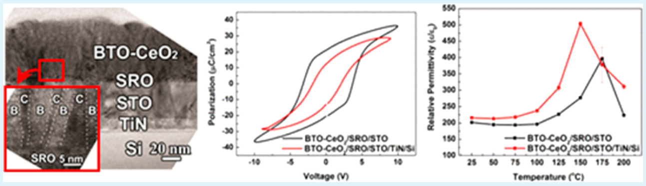

KEYWORDS: *ferroelectric, barium titanate, cerium oxide, vertically aligned nanocomposites (VAN), silicon integration*

■ INTRODUCTION

Efforts on developing lead-free materials for ferroelectric applications have gained momentum, owing largely to the great technological needs for such materials and the toxic nature of lead, along with an increasing environmental consciousness.[1−3] $BaTiO_3$ (BTO), a representative ferroelectric perovskite oxide, has long been the frontrunner among alternatives to lead-based materials in the development of thin-film ferroelectric devices. Bulk BTO exhibits a tetragonal structure at room temperature, with an in-plane lattice parameter a = 3.992 Å and out-of-plane lattice parameter c = 4.036 Å, and a remnant polarization (P_r) of about 25-27 μC/cm^2.[4] A major impediment to the implementation of BTO in ferroelectric devices has been its low Curie temperature (T_C) of 120 °C to 130 °C, where the BTO crystal structure changes from tetragonal to cubic.[4,5] As the temperature is increased, the spontaneous polarization (P_s) decreases, disappearing completely once T_C is exceeded.[4] The optimum ferroelectric response for BTO occurs when the out-of-plane film growth is c axis oriented.[6,7] In-plane compressive strain has been shown to increase the T_C as well as improve the P_r in BTO.[8]

Recently, a new method of introducing strain by incorporating a secondary phase into thin film architectures has evolved, namely self-assembled vertically aligned nanoscomposites (VANs).[9] A VAN system, a class of two phase thin-film materials, typically consists of two immiscible phases that show periodic vertical growth of alternating nanoscale heteroepitaxial domains. The unique architecture of these structures allows for precise tuning of their mechanical, electronic, and magnetic properties through vertical strain control, as well as interfacial coupling of those properties for advanced functionalities in a variety of applications like multiferroics,[10,11] spintronics,[12,13] superconductors,[14] solid oxide fuel cells,[15] and electrically tunable dielectrics.[16]

The area of electrically tunable dielectrics is a potential application for ferroelectric perovskites like BTO, owing to the variability of their dielectric constants with applied DC bias.[17] The main drawback is that ferroelectrics suffer from high dielectric losses, which can be reduced by doping or by addition of a second phase low dielectric constant material. For this purpose CeO_2, a rare-earth fluorite oxide, has long been considered as a prospective dopant in BTO.[18] BTO and CeO_2 have liquid immiscibility in the 20 to 85 % CeO_2 range,[19,20] and can both grow expitaxially on $SrTiO_3$ (STO) substrates, with cube-on-cube growth[6] and 45° in-plane rotation,[21] respectively, based on their lattice parameters (a_{BTO} = 3.992 Å; a_{CeO2} = 5.411 Å; a_{STO} = 3.905 Å). However, previous studies have shown that even small additions of CeO_2 reduce the BTO tetragonal to cubic phase transition temperature and thereby the T_C to below room temperature.[19,20,22,23] It is possible, by carefully controlling the processing conditions, that BTO and CeO_2 could still be retained as two separate phases in the same composite material, and grow epitaxially in VAN form on STO.

Most epitaxial VAN systems have been demonstrated on expensive single-crystal oxide substrates such as STO, MgO, and $LaAlO_3$, with very few exceptions.[9] Instead, it is more

Received: September 6, 2013
Accepted: November 22, 2013
Published: November 22, 2013

economically desirable to integrate the proposed BTO-CeO_2 VANs on Si substrates, which simultaneously opens up the possibility of future incorporation of VAN systems in conventional Si-based devices. Previously, epitaxial BTO thin films on Si have been demonstrated using molecular beam epitaxy and atomic layer deposition.[7,24,25] To improve the quality of BTO grown on Si, an epitaxially grown STO buffer layer can be implemented,[26−28] while a thin TiN buffer layer can be used to promote the growth of single-crystal-like epitaxial STO. In this work, ferroelectric BTO-CeO_2 VAN films have been deposited on both single crystal STO and Si substrates. In the case of the Si substrates, various buffer layer combinations, including no buffer, STO only, TiN only, and STO/TiN, have been explored to determine the best epitaxial quality of the VAN films and their ferroelectric properties. Finally, the VAN film deposition frequency was varied to determine the optimal ferroelectric properties for the VAN structures on Si.

■ EXPERIMENTAL SECTION

All films were deposited in a vacuum chamber with a base pressure of approximately 1×10^{-7} Torr at a temperature of 700 °C by pulsed laser deposition (PLD) using a Lambda Physik Compex Pro 205 KrF excimer laser (λ = 248 nm). The TiN and STO targets used for PLD were hot-pressed stoichiometric TiN and STO, respectively, purchased from Plasmaterials, Inc. The BTO-CeO_2 (1:1 molar ratio, sintered at 1200 °C) and $SrRuO_3$ (SRO) targets were custom made from powders purchased from Alfa Aesar. The substrates used for deposition were STO (001) and Si (001). The Si substrates were subjected to a 5 min buffered oxide etch to strip the native oxide prior to loading in the vacuum chamber. The TiN seed layer was deposited under vacuum at a pulse rate of 10 Hz. The STO buffer and SRO bottom electrode were deposited at a pulse rate of 5 Hz, while the deposition frequency for the BTO-CeO_2 films was varied as 2 Hz, 5 Hz, and 10 Hz, all at an optimized oxygen partial pressure of 40 mTorr.[29] Immediately following the deposition, the films were annealed at a temperature of 500 °C for 30 mins at an oxygen partial pressure of 500 Torr. 100 nm thick Au top contacts of 0.1 mm^2 area, were deposited on the BTO-CeO_2 film surface in a custom-built magnetron sputtering system using a 99.99% pure Au sputter target from Williams Advanced Materials.

X-ray diffraction (XRD) spectra were measured using a PANalytical Empyrean 2 diffractometer. Leakage current and capacitance-voltage (C−V) measurements were conducted using an Agilent E4980A Precision LCR meter. Ferroelectric polarization−electric field hysteresis (P−E) measurements were conducted on a TF Analyzer 1000 with leakage current compensation from aixACCT Systems GmbH. Transmission electron microscopy (TEM) and scanning tunneling electron microscopy (STEM) images were taken using a FEI Tecnai G2 F20 ST FE-TEM and electron diffraction images were acquired using a JEOL JEM-2010 TEM.

■ RESULTS AND DISCUSSION

First, a detailed microstructural characterization was conducted on the BTO-CeO_2 films grown on single crystalline STO substrates as a baseline study. Fig. 1 shows the XRD θ−2θ pattern of BTO-CeO_2 grown at a pulse rate of 5 Hz on single-crystalline STO substrates with an SRO bottom electrode. Clear peaks were observed for BTO ($00l$) and CeO_2 ($00l$), suggesting a preferential out-of-plane orientation of ($00l$) for both phases. No additional peaks associated with the BTO-CeO_2 system were observed, indicating that there is no intermixing between the two phases. The c value is determined to be 4.10 Å for the BTO phase. The peak position error is found to be ±144 arcsec, corresponding to a d-spacing error of ±0.002 Å. ϕ-scans, to investigate the in-plane orientation, were conducted on the BTO-CeO_2 films on STO, shown in the inset in Figure 1. A comparison of the ϕ-scans of the STO (110) and BTO (110) planes shows four small peaks for the BTO phase

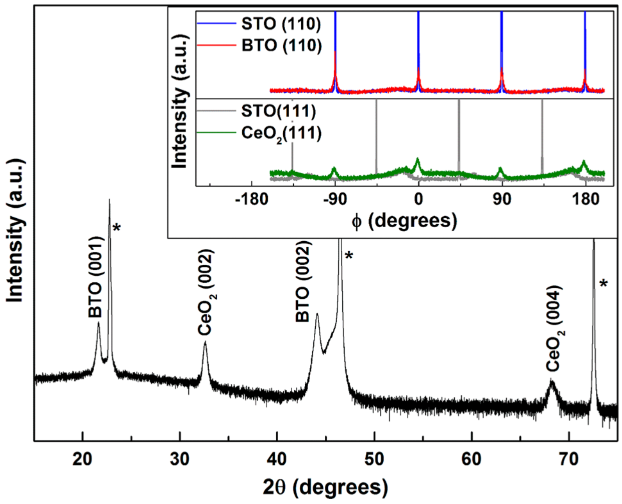

Figure 1. XRD θ−2θ scan of the for BTO-CeO_2 films grown on STO, the substrate peaks are denoted as "*". The inset shows the ϕ scan of the BTO (110) plane relative to the STO (110) plane and the CeO_2 (111) plane relative to the STO (111) plane.

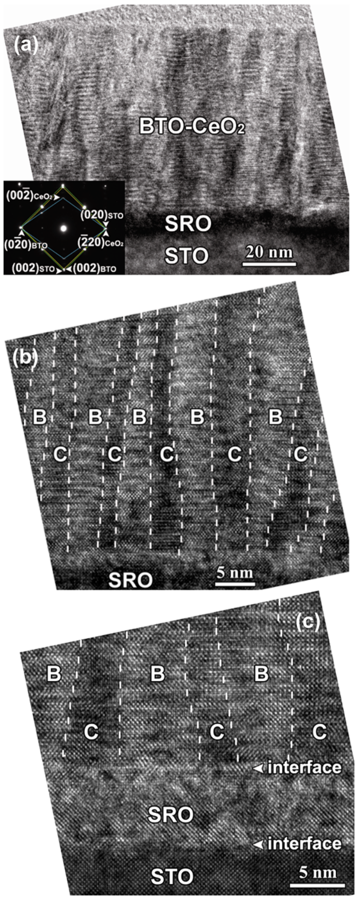

Figure 2. TEM micrographs for the BTO-CeO_2 films deposited on STO. (a) Low magnification image showing the film stack with the inset showing the corresponding SAD pattern; (b) high-resolution image showing vertically aligned nanocolumns of BTO (B) and CeO_2 (C); (c) high-resolution image of the interface between the BTO-CeO_2 film, SRO bottom electrode, and STO substrate.

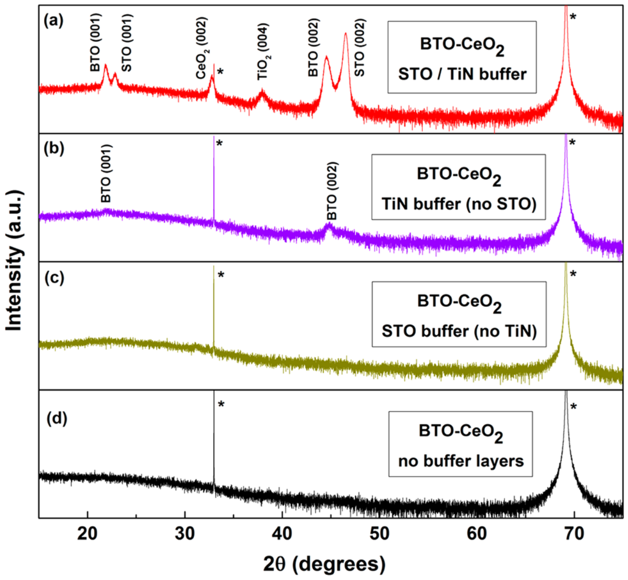

Figure 3. Comparison of the XRD θ–2θ scans for BTO-CeO_2 films deposited at 5 Hz as a function of buffer layers.

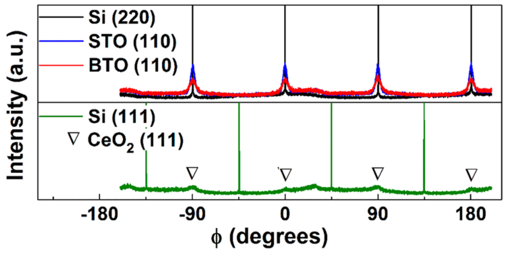

Figure 4. ϕ scan of the BTO (110) and STO (110) planes relative to the Si (110) plane and the ϕ scan of the Si (111) plane showing four small CeO_2 (111) peaks (denoted as "∇") offset 45° from the Si (111) peaks.

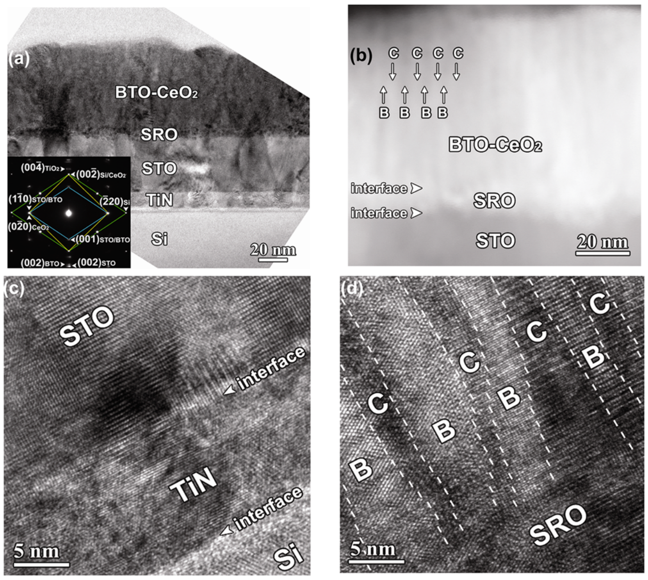

Figure 5. TEM micrographs for BTO-CeO_2 films grown on the SRO/STO/TiN/Si stack at 5 Hz. (a) Low magnification image of the film stack with the inset showing the corresponding SAD pattern; (b) STEM dark-field image showing the vertically aligned nanocolumns of BTO (B, darker contrast) and CeO_2 (C, lighter contrast); (c) high-resolution image showing the STO and TiN layers grown on the Si substrate; (d) high-resolution image showing the vertically aligned nanocolumns of BTO (B) and CeO_2 (C) on the SRO bottom electrode.

which exactly coincide with four sharp peaks for the STO substrate, indicating the cube-on-cube growth for the BTO phase as expected. From the comparison of the ϕ-scans of the STO (111) and CeO_2 (111) planes, it is evident that the four smaller peaks from the CeO_2 phase are offset from the four sharp STO peaks by exactly 45°, indicating that the CeO_2 phase has an in-plane rotation of 45° relative to the STO substrate. The in-plane orientation again shows that the BTO and CeO_2 have grown as two distinct phases and that there is no obvious intermixing between the two phases.

TEM cross-section images of the BTO-CeO_2 films grown on STO are shown in Figure 2. The low magnification image of the cross-section is shown in Figure 2 (a), with the inset showing the corresponding selected area electron diffraction (SAED) pattern. The BTO-CeO_2 layer is approximately 65 nm thick and has obvious columnar structure of the two phases. The SAED pattern shows the in-plane matching relationship to be $(010)_{BTO}\|$ $(011)_{CeO2}\|$ $(010)_{STO}$, confirming the observations in the XRD ϕ-scans in Figure 1, where BTO matches STO as cube-on-cube and CeO_2 matches with STO with a 45° in plane rotation. The *c* and *a* values for the BTO phase are determined to be 4.06 Å and 3.98 Å, respectively, suggesting in a *c*/*a* ratio of 1.02, an out-of-plane tensile strain of 0.59 % and an in-plane compressive strain of 0.3 %, compared to the bulk values of 4.036 Å and 3.992 Å for *c* and *a* (*c*/*a* ratio of 1.011). The calculation of the lattice parameters based on the TEM diffraction pattern was conducted to verify the calculations from the XRD measurements. The lattice parameters based on the XRD data should still be taken as the accurate values. The high resolution image in Figure 2b shows that the film has grown epitaxially on the thick SRO layer with distinct vertically aligned BTO and CeO_2 phases, both with column widths of 3–5 nm. The high resolution image of the film in Figure 2c of the BTO-CeO_2/SRO/STO interfaces shows that the interfaces are sharp and abrupt. The 7 nm thick SRO film grows highly epitaxially on the STO substrate, so does the nanostructured BTO-CeO_2 film.

Following the epitaxial growth of the VAN composite on STO substrates, a set of BTO-CeO_2 VAN thin films were deposited on Si substrates with various combinations of buffer layers. Figure 3 shows the XRD spectra of the BTO-CeO_2 samples deposited at 5 Hz on Si (a) with STO/TiN buffer, (b) with TiN only, (c) with STO only, and (d) without any buffer. In Figure 3a, the films on the STO/TiN buffered Si shows clear peaks for BTO (00*l*), CeO_2 (002), and STO (00*l*) peaks which, similar to the films grown directly on the STO substrate, indicates a preferential out-of-plane orientation of (00*l*) for both phases as well as the STO buffer layer. This suggests that the VAN films grown on STO/TiN buffered Si have comparable crystallinity and film quality as those on the STO substrates. No peaks associated with TiN buffer are observed, except for a small TiO_2 (004) peak, indicating that the thin TiN seed layer (10 nm) has been partially oxidized during the subsequent oxide layer growth. Among the other samples, in Figure 3b–d, only the sample with TiN buffer shows two small peaks from BTO (00*l*), whereas the sample with the STO buffer and the one without any buffer both don't show any obvious film peaks. The buffer layer study clearly suggests that the TiN seed layer serves as a critical epitaxial template for the

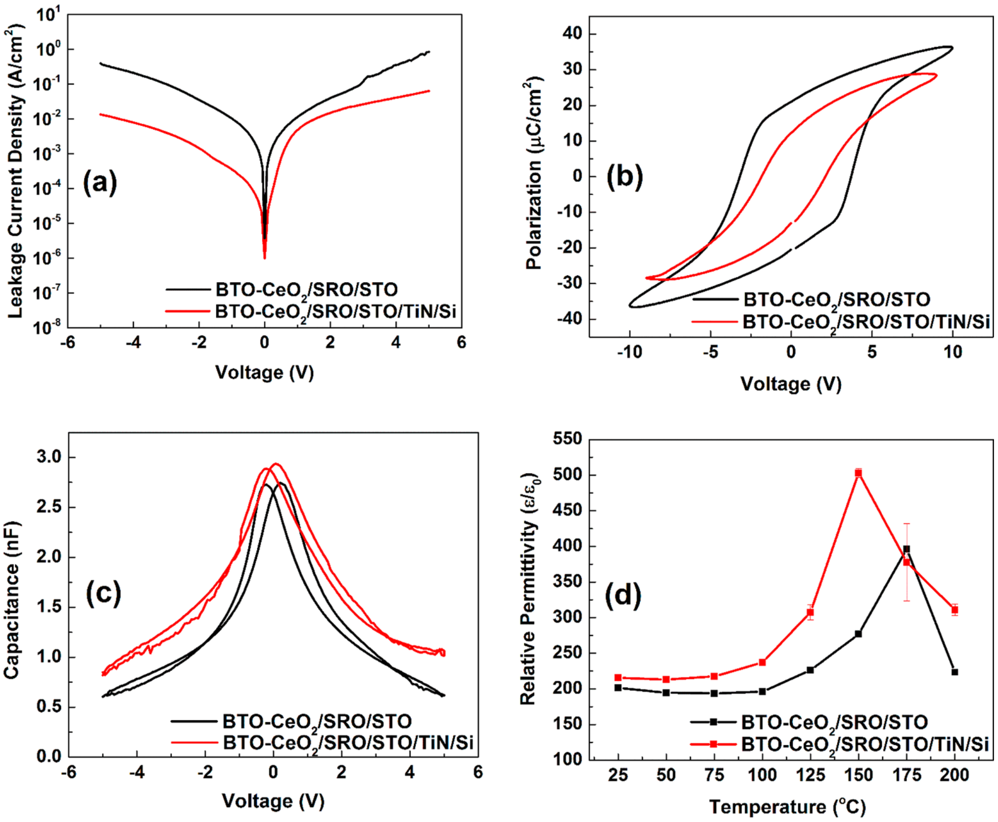

Figure 6. Electrical measurements on BTO-CeO$_2$ films deposited on STO and Si substrates: (a) leakage current, (b) polarization hysteresis at 1 kHz, (c) room-temperature capacitance–voltage curve at 10 kHz, and (d) the variation of the dielectric constant with temperature at 10 kHz.

STO buffer growth, which in turn is crucial for the highly epitaxial growth of the BTO-CeO$_2$ nanostructured film on Si. Despite the large lattice mismatch between TiN and Si (over 24%), TiN has been reported to grow on Si epitaxially through domain matching epitaxy.[30] Fig. 4 shows the ϕ-scans for the BTO-CeO$_2$ films on STO/TiN buffered Si substrates, including STO (110) and BTO (110) planes relative to the Si (110) plane and CeO$_2$ (111) relative to Si (111). This is consistent with the ϕ-scans of the samples directly grown on STO substrates, i.e., cube-on-cube growth for BTO and STO relative to the Si, and a 45° in-plane rotation between CeO$_2$ and Si.

Shown in Figure 5 are the TEM cross-section images of the BTO-CeO$_2$ films grown on STO/TiN buffered Si substrates. The low magnification cross-section TEM image is shown in Figure 5a, with the inset for the corresponding SAED pattern. The BTO-CeO$_2$ layer is approximately 65 nm thick and the STO buffer layer is approximately 40 nm thick. The distinct diffraction dots from all the film layers in the SAED pattern confirm the high-quality epitaxial growth of the buffer layers and the VAN films. The in-plane matching relationship is determined to be $(011)_{\mathrm{BTO}}\|$ $(010)_{\mathrm{CeO2}}\|(011)_{\mathrm{STO}}$ $\|(011)_{\mathrm{Si}}$ confirming the observations made in the XRD ϕ-scans in Figure 4. The c and a values for the BTO phase are determined to be 4.04 and 3.98 Å, respectively, suggesting in a c/a ratio of 1.01, an out-of-plane tensile strain of 0.1% and an in-plane compressive strain of 0.3 %. Figure 5b shows the STEM image of the sample in high angle annular dark field mode (HAADF, also called Z-contrast image, where the image contrast is proportional to $Z^{1.7}$). The BTO-CeO$_2$ film shows clear columnar growth of the BTO (darker contrast) and CeO$_2$ (brighter contrast) phases. The high resolution TEM image in Figure 5c shows the growth of the epitaxial TiN and STO buffer layers on Si substrate where the interfaces are sharp and there is no intermixing of the layers, except a thin (1–2 nm) native SiO$_x$ layer at the TiN/Si interface formed during substrate heating prior to deposition. In Figure 5d, the 7 nm thick SRO film has grown highly epitaxially on the STO buffer, which provides an epitaxial template for the BTO-CeO$_2$ film growth. The high-quality epitaxial growth of BTO and CeO$_2$ phases is evident with clear phase boundaries and the average column widths are both 3–5 nm. It is noted that compared to the BTO-CeO$_2$ films grown on STO substrates shown in Figure 2b,c, the columnar structure in the films grown on the STO/TiN buffered Si substrates are less defined. This corresponds to the higher-quality film growth observed on the STO substrates compared that on STO/TiN buffered Si, as seen in the corresponding XRD patterns Figures 1 and 3a, respectively.

Figure 6 presents a comparison study of the electrical properties measured for the BTO-CeO$_2$ films grown on STO and on Si. In Figure 6a, the leakage current for the films on both substrates is very high, with the films grown on the STO substrate showing a higher leakage than those grown on Si. Figure 6b shows the P–E curve measured on the samples at 1 kHz up to a voltage of 10 V at room temperature. In both cases, there is a distinct ferroelectric response at room temperature, indicating that the T_C is above room temperature. In the ferroelectric P–E curve, P_s is the saturation polarization value, P_r is the remnant polarization when the applied field reduced to zero, V_c and E_c are the coercive voltage and coercive field, respectively, required to force the polarization value to zero. The P_r for the films on STO is determined to be 21 μC/cm^2,

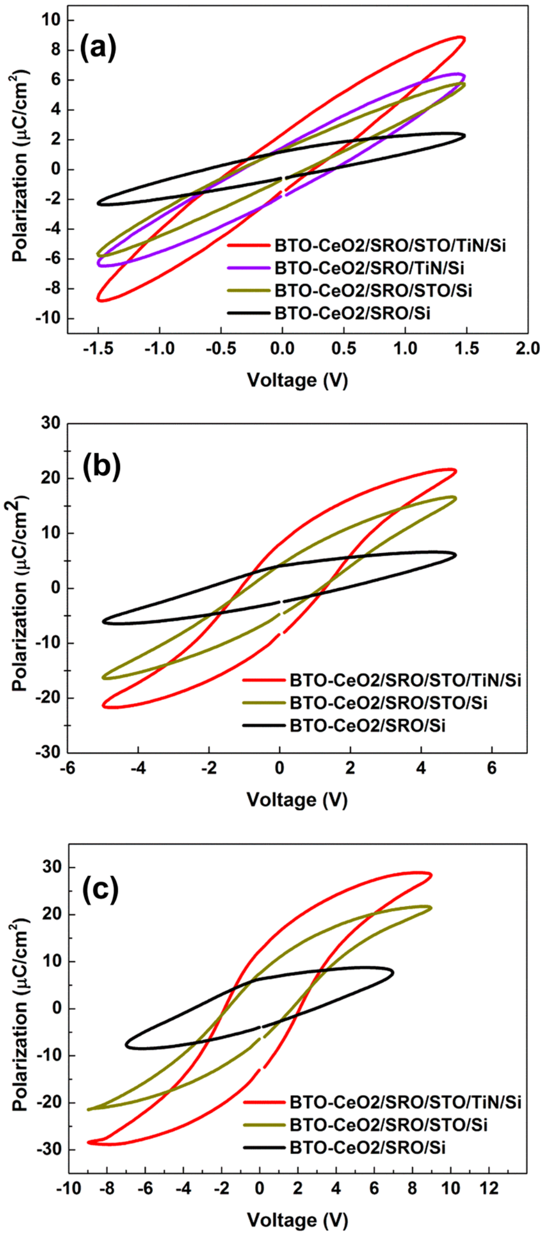

Figure 7. Comparison of the polarization hysteresis measurements for BTO-CeO_2 films deposited at 5 Hz as a function of buffer layers measured at (a) 1.5, (b) 4, and (c) 9 V.

with a coercive voltage (V_c) of 3.5 V, coercive field (E_c) of 538 kV/cm, and P_s of 37 μC/cm^2. The same parameters for the films grown on Si are 13 μC/cm^2, 2 V, 307 kV/cm, and 29 μC/cm^2, respectively. These values are consistent with the P_r of 14 μC/cm^2 and P_s of 27 μC/cm^2 measured for pure BTO films grown on STO.[29] The $C-V$ hysteresis curves in Figure 6c, measured at 10 kHz, show butterfly curves in both cases. However, the maxima of the $C-V$ curve at ±0.2 V in the case of the STO substrate and −0.2 V and 0.1 V in the case of the Si substrate, do not correspond to the V_c values observed in Figure 6b. This disparity could be attributed to artifacts due to the instrument configuration or the high leakage current, or both. Figure 6d shows the change in the measured dielectric permittivity ($\varepsilon/\varepsilon_0$) as a function of measurement temperature. The peak in the $\varepsilon/\varepsilon_0$ curve at 175 °C for the STO substrate and 150 °C for the Si substrate suggests that the T_C has increased beyond the values of 120-130 °C for bulk BTO. This suggests that the incorporation of CeO_2 with BTO in VAN form presents a promising approach for increasing T_C of BTO.

The $P-E$ measurements for the VAN films deposited on Si with various buffer layers are presented in Figure 7. Compared to the sample deposited on the STO/TiN/Si stack, the sample without the buffer layers shows no ferroelectric response, and the hysteresis loop is characteristic of a lossy dielectric. Oddly however, the sample deposited without the TiN seed layer also shows a ferroelectric response, though not as good as that of the sample grown on the STO/TiN/Si stack. It is possible that there may be some localized ordering in the STO layer that has prompted some local texturing of the BTO phase, not obvious through the XRD characterization. It is also interesting to note that despite the lack of obvious texturing in the samples with only STO buffer, the ferroelectric response implies that there is no intermediate phase formation between the BTO and CeO_2 regardless of the presence of buffer layers.

In addition to the effect of the buffer layers, the deposition frequency also has a strong impact on the epitaxial growth of the BTO-CeO_2 films as well as their ferroelectric properties. Shown in Figure 8 is the XRD data for BTO-CeO_2 films, all approximately 65 nm thick, grown on the STO/TiN/Si stack as a function of deposition frequency. Figure 8a−c show the data for the samples deposited at 5 Hz, 2 Hz, and 10 Hz, respectively. All three samples show distinct BTO, STO, and CeO_2 (00*l*) peaks. Upon closer examination of the BTO (001) peak position in Figure 8d, there appears to be a correlation between the deposition frequency and the BTO (001) peak

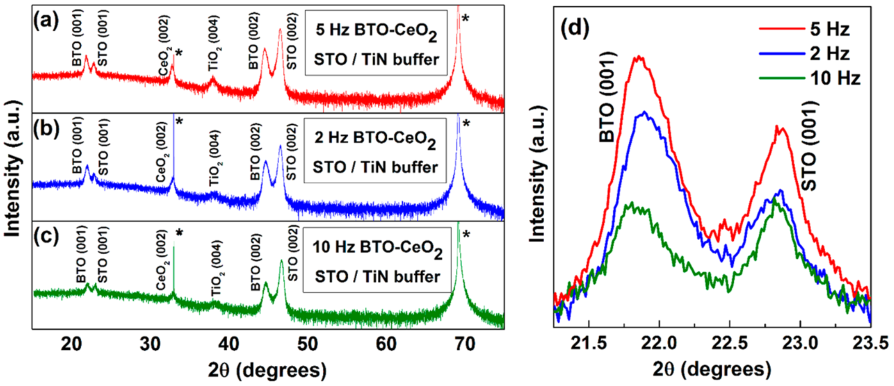

Figure 8. Comparison of the XRD $\theta-2\theta$ scans for BTO peak for the BTO-CeO_2 films deposited on the SRO/STO/TiN/Si stack at (a) 5, (b) 2, and (c) 10 Hz; (d) position of the BTO (001) peak as a function of deposition frequency.

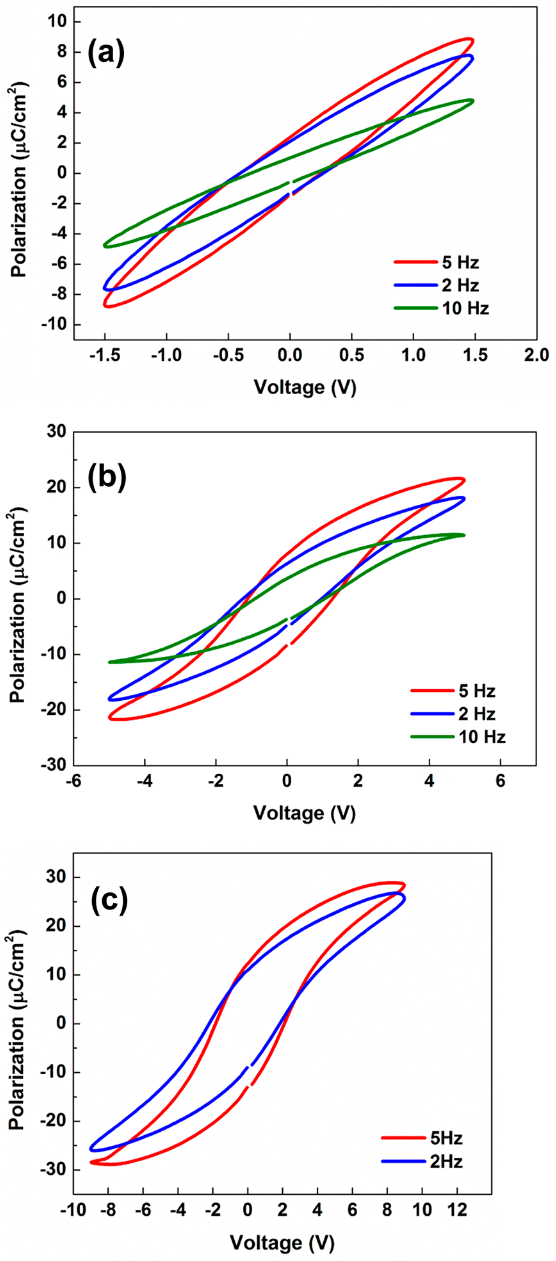

Figure 9. Comparison of the polarization hysteresis measurements for BTO-CeO_2 films deposited on the SRO/STO/TiN/Si stack as a function of deposition frequency measured at (a) 1.5, (b) 4, and (c) 9 V.

position. The peak for the 10 Hz sample has the smallest 2θ position, followed by the 5 Hz sample, and then the 2 Hz sample, corresponding to *c* value of 4.07, 4.06, and 4.06 Å, respectively. The corresponding out-of-plane tensile strain is calculated to be 0.81, 0.68, and 0.52%, respectively. The full width at half maximum (FWHM) for the BTO (001) peak is measured to be 0.293, 0.329, and 0.361° for the 5, 2, and 10 Hz samples, respectively. It is expected that, on the basis of the *c* value and out-of-plane strain, the 10 Hz sample should have the best ferroelectric response. However, from the *P*−*E* measurement data in Figure 9, the 5 Hz sample still shows the best ferroelectric response, closely followed by the 2 Hz sample, while the response of the 10 Hz sample is much poorer, which directly correlates to their FWHM values. This shows that 5 Hz is the optimum deposition frequency to achieve the best epitaxial quality of the BTO-CeO_2 films on the SRO/STO/TiN/Si stack, resulting in the optimum ferroelectric response.

The data presented so far show that the ferroelectric properties of the BTO-CeO_2 films deposited on STO substrates are comparable to reports of pure BTO deposited on STO substrates.[29,31,32] The ferroelectric response of the BTO-CeO_2 films deposited on Si is slightly lower than, but still in the same range as that of the BTO-CeO_2 films on STO. The FWHM of 0.263° for the films grown on the STO substrate is close to, but still better than that of any of the films grown on Si, indicating that the quality of the films on the STO substrate are slightly better than those grown on Si. This can be attributed to the quality of the STO buffer layer compared to the STO substrates; improving the epitaxial quality of this layer will most likely improve the ferroelectric response of the films deposited on Si substrates. It must be noted, moreover, that the properties of BTO-CeO_2 films deposited on Si are also comparable to those of BTO and other BTO-based materials deposited on Si.[33−36]

Another remarkable property of BTO-CeO_2 composite thin films is the exhibition of ferroelectric properties at and beyond room temperature, despite the high concentration of CeO_2. However, in previous reports, CeO_2 has been shown to decrease the tetragonal to cubic phase transition temperature and hence the T_C in BTO.[19,20,22,23] Even in a vertically oriented BTO and CeO_2 composite, the T_C was reported to steadily decrease with increasing concentrations of CeO_2, down to as low as −80 °C.[37] Increasing the CeO_2 concentration in BTO was found to cause an expansion of the *a* axis, a shrinking of the *c* axis, resulting in a net decrease in the *c*/*a* ratio, which was believed to be caused because of Ce substitution of Ba in the BTO lattice.[18,38,39] It was determined that in reducing environments above 1250 °C, CeO_2 undergoes a chemical change to Ce_2O_3, where the stable tetravalent Ce^{4+} state changes to Ce^{3+}, which is responsible for the substitution of the Ba.[39] Most of these previous reports involved processing temperatures far beyond 1250 °C. A high temperature processing step in target preparation could result in a reaction involving the Ba and Ce and thus any films deposited using that target would be affected accordingly.

Conversely, in our case, the sintering temperature for the composite target was maintained at 1200 °C, preventing Ce/Ba substitution reaction from occurring. The *c*/*a* ratios for the BTO-CeO_2 films grown on STO and STO/TiN buffered Si are 1.02 and 1.01, respectively, which shows that tetragonality is maintained in the BTO at room temperature. Previously, VAN structures of BTO-Sm_2O_3[40] and $Ba_{0.6}Sr_{0.4}TiO_3$−Sm_2O_3[16] on STO substrates both show an increased T_C, where the onset of the tetragonal to cubic phase transition was delayed in the strained BTO matrix by the considerably harder Sm_2O_3 phase. CeO_2 has a reported elastic modulus in the range of 112 to 264 GPa,[41] so it serves a similar function as the Sm_2O_3 (elastic modulus of 125 GPa[40]) described above. Thus, the retention of ferroelectric properties at room temperature is due to the processing conditions of the composite target, whereas the extension of the T_C beyond the bulk value can be attributed to the strained configuration owing to the VAN structure. More excitingly, this work demonstrates that these properties can be maintained for the BTO-CeO_2 VAN samples grown on STO/TiN buffered Si substrates, facilitating the prospect of integrating nanostructured ferroelectrics in Si-based devices.

CONCLUSIONS

We have successfully demonstrated, for the first time, a room temperature ferroelectric response in BTO-CeO_2 1:1 molar ratio composites, and an increase in the T_C to at least 150 °C because of the strained VAN structure. The BTO-CeO_2 films grow in a VAN architecture of 3−5 nm column widths on TiN/STO buffered Si substrates. The BTO-CeO_2 composite shows no Ce substitution of the Ba in the BTO lattice, no obvious intermixing, and no intermediate phase formation. The TiN seed layer protects the underlying Si substrate from oxidation, while providing a template for the near epitaxial growth of the STO buffer layer as well as a highly epitaxial VAN structure. These results show that by precise tailoring of processing and deposition conditions, it is possible to improve the ferroelectric response and the T_C of the BTO-CeO_2 system. Moreover, by careful selection of buffer layers, the integration of high-quality functional VAN architectures on Si substrates is highly feasible, opening the door to future incorporation of functional oxide materials in conventional Si-based devices.

AUTHOR INFORMATION

Corresponding Author

*E-mail: wangh@ece.tamu.edu.

Notes

The authors declare no competing financial interest.

ACKNOWLEDGMENTS

This work was funded by the U.S. National Science Foundation (NSF-1007969).

REFERENCES

(1) Rodel, J.; Jo, W.; Seifert, K. T. P.; Anton, E. M.; Granzow, T.; Damjanovic, D. *J. Am. Ceram. Soc.* **2009**, *9*, 1153−1177.

(2) Panda, P. K. *J. Mater. Sci.* **2009**, *44*, 5049−5062.

(3) Leontsev, S. O.; Eitel, R. E. *Sci. Technol. Adv. Mater.* **2010**, *11*, 044302.

(4) Uchino, K., *Ferroelectric Devices*; CRC Press: Boca Raton, FL, 2010.

(5) Haertling, G. H. *J. Am. Ceram. Soc.* **1999**, *82*, 797−818.

(6) Lin, W. J.; Tseng, T. Y.; Lu, H. B.; Tu, S. L.; Yang, S. J.; Lin, I. N. *J. Appl. Phys.* **1995**, *77*, 6466−6471.

(7) Vaithyanathan, V.; Lettieri, J.; Tian, W.; Sharan, A.; Vasudevarao, A.; Li, Y. L.; Kochhar, A.; Ma, H.; Levy, J.; Zschack, P.; Woicik, J. C.; Chen, L. Q.; Gopalan, V.; Schlom, D. G. *J. Appl. Phys.* **2006**, *100*, 024108.

(8) Choi, K. J.; Biegalski, M.; Li, Y. L.; Sharan, A.; Schubert, J.; Uecker, R.; Reiche, P.; Chen, Y. B.; Pan, X. Q.; Gopalan, V.; Chen, L. Q.; Schlom, D. G.; Eom, C. B. *Science* **2004**, *306*, 1005−1009.

(9) Zhang, W.; Chen, A.; Bi, Z.; Jia, Q.; MacManus-Driscoll, J. L.; Wang, H. *Curr. Opin. Solid State Mater. Sci.* **2013**.

(10) Chen, A. P.; Bi, Z. X.; Jia, Q. X.; MacManus-Driscoll, J. L.; Wang, H. Y. *Acta Mater.* **2013**, *61*, 2783−2792.

(11) Zheng, H.; Wang, J.; Lofland, S. E.; Ma, Z.; Mohaddes-Ardabili, L.; Zhao, T.; Salamanca-Riba, L.; Shinde, S. R.; Ogale, S. B.; Bai, F.; Viehland, D.; Jia, Y.; Schlom, D. G.; Wuttig, M.; Roytburd, A.; Ramesh, R. *Science* **2004**, *303*, 661−663.

(12) Chen, A. P.; Bi, Z. X.; Tsai, C. F.; Lee, J.; Su, Q.; Zhang, X. H.; Jia, Q. X.; MacManus-Driscoll, J. L.; Wang, H. Y. *Adv. Funct. Mater.* **2011**, *21*, 2423−2429.

(13) Zhang, W. R.; Chen, A. P.; Khatkhatay, F.; Tsai, C. F.; Su, Q.; Jiao, L.; Zhang, X. H.; Wang, H. Y. *ACS Appl. Mater. Interface* **2013**, *5*, 3995−3999.

(14) Tsai, C. F.; Chen, L.; Chen, A. P.; Khatkhatay, F.; Zhang, W. R.; Wang, H. Y. *IEEE Trans. Appl. Supercond.* **2013**, *23*, 8001204.

(15) Su, Q.; Yoon, D.; Chen, A. P.; Khatkhatay, F.; Manthiram, A.; Wang, H. *J. Power Sources* **2013**, *242*, 455−463.

(16) Lee, O.; Harrington, S. A.; Kursumovic, A.; Defay, E.; Wang, H. Y.; Bi, Z. X.; Tsai, C. F.; Yan, L.; Jia, Q. X.; MacManus-Driscoll, J. L. *Nano Lett.* **2012**, *12*, 4311−4317.

(17) Kong, L. B.; Li, S.; Zhang, T. S.; Zhai, J. W.; Boey, F. Y. C.; Ma, J. *Prog. Mater. Sci.* **2010**, *55*, 840−893.

(18) Issa, M. A. A.; Molokhia, N. M.; Dughaish, Z. H. *J. Phys. D: Appl. Phys.* **1983**, *16*, 1109−1114.

(19) Guha, J. P.; Kolar, D. *J. Am. Ceram. Soc.* **1973**, *56*, 5−6.

(20) Guha, J. P. *J. Am. Ceram. Soc.* **1979**, *62*, 627−628.

(21) Kim, Y. J.; Gao, Y.; Herman, G. S.; Thevuthasan, S.; Jiang, W.; McCready, D. E.; Chambers, S. A. *J. Vac. Sci. Technol., A* **1999**, *17*, 926−935.

(22) Dubuisson, J.; Basseville, P. In *Proceedings of the Materials Science Research Conference*; North Carolina State University, Raleigh, NC, Nov 16−18, 1964 ; Kriegel, W. W., Palmour, H., III, Eds.; Plenum Press: New York, 1966.

(23) Hwang, J. H.; Han, Y. H. *Jpn. J. Appl. Phys., Part 1* **2000**, *39*, 2701−2704.

(24) Warusawithana, M. P.; Cen, C.; Sleasman, C. R.; Woicik, J. C.; Li, Y. L.; Kourkoutis, L. F.; Klug, J. A.; Li, H.; Ryan, P.; Wang, L. P.; Bedzyk, M.; Muller, D. A.; Chen, L. Q.; Levy, J.; Schlom, D. G. *Science* **2009**, *324*, 367−370.

(25) Abel, S.; Caimi, D.; Sousa, M.; Stoferle, T.; Rossel, C.; Marchiori, C.; Chelnokov, A.; Fompeyrine, J. *Proc. SPIE* **2012**, *8263*, 82630Y.

(26) Sanchez, F.; Varela, M.; Queralt, X.; Aguiar, R.; Morenza, J. L. *Appl. Phys. Lett.* **1992**, *61*, 2228−2230.

(27) Shih, W. C.; Yang, W. H. *Physica B* **2010**, *405*, 234−238.

(28) Niu, G.; Penuelas, J.; Largeau, L.; Vilquin, B.; Maurice, J. L.; Botella, C.; Hollinger, G.; Saint-Girons, G. *Phys. Rev. B* **2011**, *83*, 054105.

(29) Chen, A. P.; Khatkhatay, F.; Zhang, W.; Jacob, C.; Jiao, L.; Wang, H. *J. Appl. Phys.* **2013**, *114*, 124101.

(30) Wang, H.; Kvit, A.; Zhang, X.; Koch, C. C.; Narayan, J. *MRS Proc.* **2001**, *697*, P8.4.

(31) Li, T. X.; Hu, Z.; Zhang, M.; Li, K. S.; Yu, D. B.; Yan, H. *Appl Surf Sci* **2012**, *258* (10), 4558−4562.

(32) Ramana, E. V.; Yang, S. M.; Jung, R. J.; Jung, M. H.; Lee, B. W.; Jung, C. U. *J. Appl. Phys.* **2013**, *113*, 187219.

(33) Shin, J.; Goyal, A.; Jesse, S.; Kim, D. H. *Appl. Phys. Lett.* **2009**, *94*, 252903.

(34) Fasquelle, D.; Mascot, M.; Carru, J. C. *Solid State Electron* **2012**, *75*, 6−12.

(35) George, J. P.; Beeckman, J.; Woestenborghs, W.; Smet, P. F.; Bogaerts, W.; Neyts, K. *Nanoscale Res. Lett.* **2013**, *8*, 1−7.

(36) Zhou, Q.; Zhou, C. R.; Yang, H. B.; Chen, G. H.; Li, W. Z.; Wang, H. *J. Am. Ceram. Soc.* **2012**, *95*, 3889−3893.

(37) Yamada, T.; Sandu, C. S.; Gureev, M.; Sherman, V. O.; Noeth, A.; Muralt, P.; Tagantsev, A. K.; Setter, N. *Adv. Mater.* **2009**, *21*, 1363−1367.

(38) Cernea, M.; Matei, I.; Iuga, A.; Logofatu, C. *J. Mater. Sci.* **2001**, *36*, 5027−5030.

(39) Hennings, D. F. K.; Schreinemacher, B.; Schreinemacher, H. *J. Eur. Ceram. Soc.* **1994**, *13*, 81−88.

(40) Harrington, S. A.; Zhai, J. Y.; Denev, S.; Gopalan, V.; Wang, H. Y.; Bi, Z. X.; Redfern, S. A. T.; Baek, S. H.; Bark, C. W.; Eom, C. B.; Jia, Q. X.; Vickers, M. E.; MacManus-Driscoll, J. L. *Nat. Nanotechnol.* **2011**, *6*, 491−495.

(41) Wachtel, E.; Lubomirsky, I. *Scr. Mater.* **2011**, *65*, 112−117.